Blister-dominated retention mechanism in tungsten exposed to high fluence deuterium plasma

Mi Liu[a,b], Wangguo Guo[a,b], Long Cheng[a,b *], Jun Wang[c], Shiwei Wang[a,b], Hao Yin[a,b], Ting Wang[a,b], Yuhua Huang[a,b], Yue Yuan[a,b], Thomas Schwarz-Selinger[d], Gregory De Temmerman[e], Xing-Zhong Cao[f], G.-N. Luo[g], Guang-Hong Lu[a,b]

[a] *School of Physics, Beihang University, Beijing, 100191, China*

[b] *Beijing Key Laboratory of Advanced Nuclear Materials and Physics, Beihang University, Beijing, 100191, China*

[c] *State Key Laboratory of Optoelectronic Materials and Technologies, School of Physics, Sun Yat-sen University, Guangzhou, 510275, China*

[d] *Max-Planck-Institut für Plasmaphysik, Garching, 85748, Germany*

[e] *ITER Organization, Route de Vinon sur Verdon, CS90 046, F-13067 St Paul Lez Durance Cedex, France*

[f] *Institute of High Energy Physics, Chinese Academy of Sciences, Beijing, 100049, China*

[g] *Institute of Plasma Physics, Chinese Academy of Sciences, Hefei, 230031, China*

Email: LCheng@buaa.edu.cn

Abstract:

To investigate the role of blister formation on hydrogen isotopes retention, a series of deuterium plasma exposures with high fluences up to 1.0×10^{28} ions/m^2 were performed using recrystallized tungsten samples at 500 K in the linear plasma device STEP. Increases of blister density and deuterium retention are observed with increasing plasma fluence. According to the simulation of thermal desorption spectrum, it is suggested that the increase of total deuterium retention is mainly attributed to the production of irradiation-induced defects with certain depth profiles, rather than intrinsic defects. The irradiation-induced defects are suggested to be dislocation-type defects and vacancy-type defects created by blistering and contribute to the majority of total deuterium retention. A blister-dominated retention mechanism is proposed to describe hydrogen isotopes retention in conditions when blistering is severe as in this study.

Keywords: tungsten; deuterium plasma; high fluence; blister; deuterium retention

1. Introduction

Tungsten (W) is one of the main candidates for plasma-facing materials (PFM) in future nuclear fusion devices [1]. As such, the W material will be exposed to high fluxes of hydrogen isotopes (HI) plasma which causes HI retention in W and material modifications [2]. Tritium (T) retention is a well known but key issue, which would reduce fuel utilizing efficiency and give rise to a radioactive risk and safety concerns. Therefore, understanding HI retention mechanism in W is of great importance to predict HI retention behavior and even provide a reference for designing advanced PFM to reduce retention.

Due to the very low solubility of HI in W, HI retention in W is mainly determined by HI trapped at intrinsic and irradiation-induced defects [3]. The retention is usually described based on a diffusion-limited trapping mechanism in which the trapping of HI by defects is limited by the depth reached by the diffusive HI. In ITER, extremely high plasma fluences will be accumulated at the striking point and expected to be in excess of 10^{30} m^{-2} [2] which was recently achieved in linear plasma device Magnum-PSI [4]. In the high plasma fluence regime, it is suggested that HI trapped at bulk defects including intrinsic defects and neutron-induced defects (not discussed in this work) may dominate the retention compared to plasma irradiation-induced defects, because the irradiation-induced defects created by HI plasma are usually limited to the near surface region of a few μm (thus limited trap sites for HI) [3]. Due to the high mobility of HI, the diffusion depth of HI is usually much larger than the depth where irradiation-induced defects are produced. Therefore, the increase of HI retention dominated by intrinsic defects is approximately proportional to the square root of plasma fluence Φ (or exposure time t), i.e., $\Phi^{0.5}$ (or $t^{0.5}$) [3]. A large amount of data about the relationship between HI retention and fluence have been summarized in [3], which qualitatively satisfies $\Phi^{0.5}$ thus meeting the expectation of a diffusion-limited process, such as the filling of intrinsic defect sites by the diffusion of solute through the material. However, D retention in some works [5,6] with high fluences shows a trend of saturation with increasing fluence. This implies that irradiation-induced defects such as blisters could affect retention in certain conditions. The cavity of a blister can store D_2 and contribute to retention [7]. Recently a high density of dislocations as

irradiation-induced defects are observed in the vicinity of blisters [8,9] and investigations indicate that dislocations can trap D to increase retention [10–12]. Therefore, the role of blister formation on retention requires a careful examination.

In this work, a dedicated experiment was carried out to examine the role of blisters on D retention. At 500 K, a series of D plasma exposures with various fluences were performed using recrystallized W samples. The highest fluence, reached by operating the linear plasma device for continuous 64 hours, was 1.0×10^{28} ions/m^2. Surface blistering was characterized and D retention was measured. By investigating the simulated results of thermal description spectra with the help of TMAP and defects characterization, it is suggested that the increase of total retention with fluence is dominated by the increase of blister-induced defects in the surface layer of a certain thickness, instead of by the filling of intrinsic defects during D diffusion towards the bulk. Interestingly, our simulation results suggest that blister-induced defects, especially dislocations, are diffusive and of a depth distribution up to tens of microns, which have a strong impact on retention.

2. Experimental details

2.1. Sample preparation

Samples were taken from a rolled polycrystalline W sheet with a 99.95 wt.% purity purchased from Advanced Technology and Materials Co., Ltd [13]. The dimension of the samples was $10\times10\times1$ mm^3. They were mechanically grinded by SiC sandpapers and then recrystallized at 1973 K for 1 hour (h) in vacuum (~10^{-3} Pa). Finally, they were electrochemically polished with a sodium hydroxide solution until the surface showed a mirror finish. The surface morphology after preparation is shown in figure 1. Electron backscattered diffraction was applied to scan the surface and the average grain size of ~37.7 μm was determined by the analysis software package Channel 5, in which the grains were separated by grain boundaries with misorientation angles greater than 15 degree.

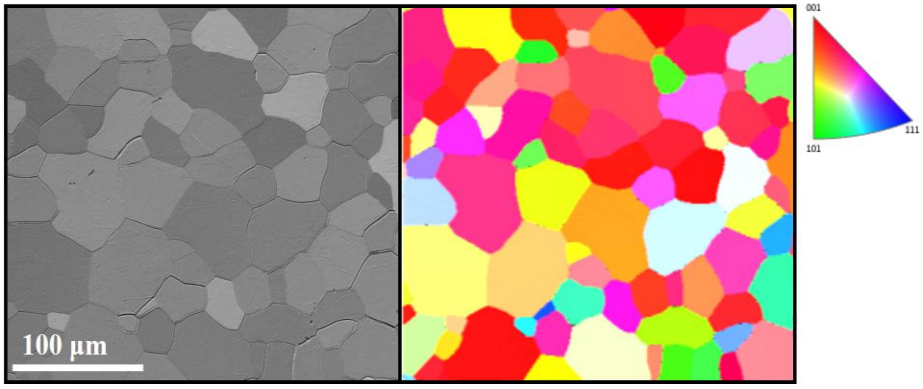

Figure 1. Surface morphology (left) and surface normal direction IPF map (right) of an as-prepared recrystallized W sample. The average grain size is ~37.7 μm measured by EBSD mapping.

In order to observe the microstructure of blister-induced defects, transmission electron microscope (TEM) specimens were prepared. The raw TEM specimens are 3 mm in diameter and 170 μm in thickness cut from a W foil provided by the same supplier as mentioned above. Specimens were first mechanically polished to a thickness of 70 μm. Then they were recrystallized and electrochemically polished with identical parameters as bulk samples to reach a mirror-like surface. The pristine microstructure of the specimen after preparation is close to that of the bulk samples. After plasma exposure, the specimens were prepared using a twin-jet electro polisher (Struers TenuPol-5). With the exposed surface side covered by paraffin, the specimen was back-thinned using sodium hydroxide solution at room temperature, and then a perforation was generated at the center of the sample. Finally, the paraffin on the exposed surface was cleaned using acetone. For observing the microstructure and defects around blisters, both sides of the sample were electrochemically polished again to reduce the thickness of the exposed surface by ~1 μm, estimated by integrating the polishing time with the thinning rate of a reference specimen.

2.2. Deuterium plasma exposure

The recrystallized W samples were exposed to D plasma in the linear plasma device STEP located at Beihang university [14,15]. STEP was operated at a high flux of about 4.4×10^{22} $m^{-2}s^{-1}$ measured by a Langmuir probe located 3.5 cm in front of the sample surface [13]. The exposure durations were 2, 8, 16, and 64 h, which resulted in fluences of 3.2×10^{26}, 1.3×10^{27},

2.5×10^{27}, and 1.0×10^{28} ions/m^2, respectively. Hereinafter, these samples are referred to as 2h_sample, 8h_sample, 16h_sample, and 64h_sample, respectively. The incident D ion energy was set to ~40 eV by applying a negative biasing voltage to the sample. During exposure, the sample temperature was about 500 K, and was monitored by a K-type thermocouple touching the rear of the sample.

The TEM specimen was exposed to D plasma with exposure parameters identical to that for bulk samples except for the fluence. The TEM specimen temperature was about 550 K as measured by the thermocouple press at the rear of the specimen. The purpose of TEM specimen exposure was to create blisters to characterize the microstructure of blister-induced defects. For the sake of TEM observation in a limited field of view, small blisters were needed which requires a low fluence of 1.0×10^{26} ions/m^2 compared to that of bulk samples.

2.3. Analysis and characterization methods

After D irradiation and before thermal desorption, surface morphology modifications of the samples were observed by scanning electron microscopy (SEM, ZEISS Gemini 300). Cross-sections of blisters were prepared using a focused ion beam combined with SEM imaging (FIB-SEM, ZEISS Crossbeam 540) to unfold the sub-surface morphology under the blisters. During the observation, the target stage was tilted at an angle of 54 degree. Before and after plasma exposure, the TEM specimens were observed by employing JEOL JEM 2100 and FEI TECNAI G^2 20 with a 200 kV acceleration voltage.

Nuclear reaction analysis (NRA) using the D(^{3}He,p)^{4}He nuclear reaction was performed for the measurement of D depth profile in the samples at IPP-Garching [16]. The ^{3}He beam with a spot size of 1 mm^2 was positioned in the sample center. ^{3}He energies ranging from 0.5 to 4.5 MeV were applied to probe the samples down to ~7 μm. Emitted protons were detected at a scattering angle of 135° for all energies in addition to alphas under a scattering angle of 102° for energies below 1.2 MeV. Decomposition of the measured proton and alpha spectra was performed with the NRADC software [17] to derive the most probable D concentration as a function of depth.

D desorption from W samples was measured by thermal desorption spectroscopy (TDS) at Beihang University [18]. The time lag between the plasma exposure and TDS measurement

was at least one month to ensure the release of interstitial D atoms. The sample was placed in a vacuum chamber with a base pressure of about 1×10^{-6} Pa. The sample was heated up to 1273 K by a W rod heater under the sample at a constant ramping rate of 1 K/s. The sample temperature was monitored by a W-25Re thermocouple contacting the rear of the sample. A quadrupole mass spectrometer (MKS Microvision Plus) detected the mass 4 and 3 (D_2 and HD) signals, the absolute sensitivity of which was calibrated using a standard leak (VTI). The total D retention consists of both D_2 and HD and the contribution of HD is usually less than 10%.

The tritium migration analysis program (TMAP) code was used to simulate the TDS and give information about D diffusion and trapping by defects in this study. It computes the time evolution of HI species depth and concentration in a one-dimensional system with a preset defect distribution. The TMAP code has been described in detail in [19]. The code has been widely used to simulate HI irradiation and desorption in W [20–26]. In this study, the diffusion coefficient was taken from Frauenfelder [27] after the mass correction. The corrected diffusion coefficient is $D_D= 2.9\times10^{-7}$ exp(-0.39 eV/kT) [m^2/s], where k is the Boltzmann constant and T is the temperature [26]. As HI release from W surface is rapid, the surface D concentration is set to be zero as a boundary condition, $C^{sol}(0,t) \equiv 0$ [20,21,28–30]. The assumption of single atom occupancy of a trap is adopted in TMAP. DFT calculations [31,32] show that multiple atoms occupancy in a trap and the detrapping energy is filling-level dependent. However, the two assumptions of single and multiple occupancy can only be discerned in experiment of isotope exchange at low temperature. For other cases, the single occupancy assumption does suffice to describe H trapping [3,33]. Besides, traps were assumed to be saturated with D atoms, thus the D depth profile represents the trap depth profile.

Positron annihilation doppler broadening (PADB) was used to detect vacancy-type defects [34–37] at Key Laboratory of Nuclear Techniques Multi-research Center, Institute of High Energy Physics, Chinese Academy of Sciences [38]. The measurement was carried out at room temperature with an energy-variable slow positron beam. Positrons were produced by adopting a ^{22}Na radioactive source and then projected into W material. The mean incident depth of positron, R (nm), was calculated by $R = (A/\rho)E^n$, in which E (keV) stands for the positron incident energy, ρ (g/cm^3) is the material density (19.35 g/cm^3 for W), and A and n (nth power) are constants depending on the given material. Here, for W, A and n are 40 and 1.6,

respectively. The positron incident energy ranged from 0.18 to 25.18 keV, thus corresponding to a depth of 0.1–360.6 nm. In the annihilation reaction between a positron and an electron, gamma rays with energies of 499.5–522.5 keV were probed by a high-purity Ge detector. In the obtained doppler broadening spectra, the S parameter is determined by the ratio of the central spectra area (510.2–511.8 keV) to the whole spectrum area (499.5–522.5 keV). The S parameter is related to the positron annihilation with valence electron, thus sensitive to defects with an open volume such as vacancy-type defects [34]. The S increase indicates the increase of vacancy-type defect concentration.

3. Results

3.1.Surface blistering

Surface blistering dominates the surface morphology change after plasma exposure as shown in figure 2. It is evident that the density of blisters develops with increasing fluence. The blister size remains relatively constant below 10 μm, but the blister shape varies with fluence. In the 2h_sample and 8h_sample, blisters have elliptic and domed shapes. A small number of blisters are burst with a hole at the edge of the blister cap. For 16h_sample and 64h_sample, blisters are mostly irregular and burst. Besides, small material extrusions such as fissures on the surface are found in the case of 16 h and 64 h exposure.

A blister is usually associated with a crack or cavity beneath the surface. The characteristic of the crack is observed in two typical types of blisters found on 64h_sample via the cross-section prepared by FIB. In figure 3(a) the crack is right beneath the surface, which has been widely observed in literature [5,18,39,40]. While the crack in figure 3(b) is found to be perpendicular to the surface, it is suggested that this crack is part of the blister nearby, which is identified as a small extrusion in the view of the top surface. Both of the cracks are located at a depth of 5 μm from the surface.

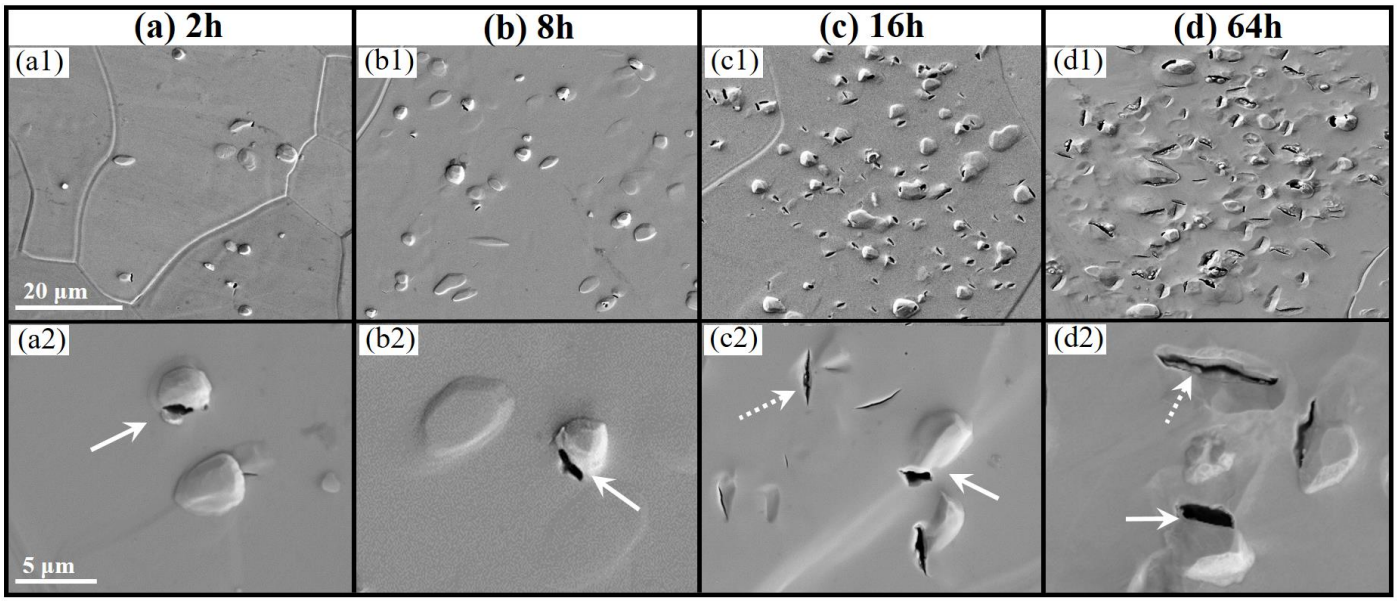

Figure 2. SEM images of recrystallized samples exposed to D plasma at 500 K with various exposure durations/fluences. They were exposed to (a) 2 h (3.2×10^{26} ions/m^2), (b) 8 h (1.3×10^{27} ions/m^2), (c) 16 h (2.5×10^{27} ions/m^2), and (d) 64 h (1.0×10^{28} ions/m^2), respectively. The images in the same row were taken at the same magnification. The burst blisters with broken edges are indicated by solid arrows. Small material extrusions such as fissures are indicated by dashed arrows.

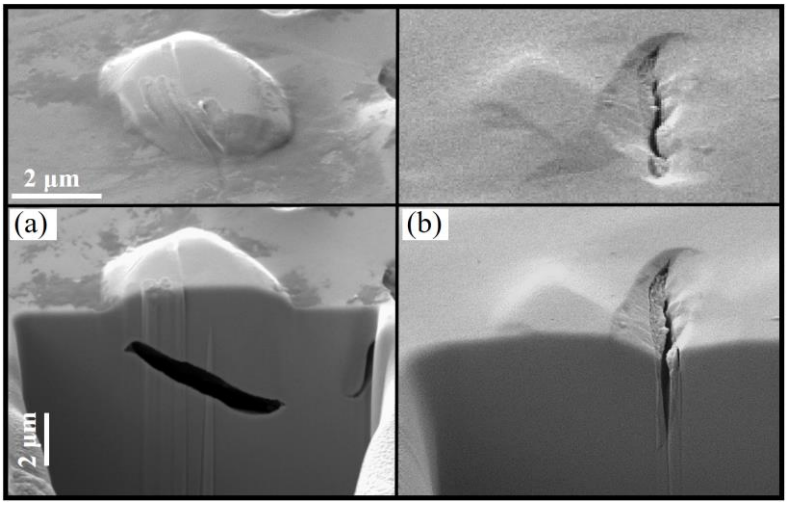

Figure 3. Cross-sections of blisters prepared by FIB from the sample exposed to plasma for 64 h. The target stage was tilted at an angle of 54 degree.

3.2.Deuterium depth profile

Figure 4 shows the depth profiles of D concentration in the W samples after plasma exposure as derived by NRA. D retention within the first 7 μm is calculated by summing D concentration

over the depth, which is $(6.0\pm0.9)\times10^{19}$ D/m^2, $(1.1\pm0.1)\times10^{20}$ D/m^2, $(1.0\pm0.2)\times10^{20}$ D/m^2, and $(3.5 \pm 0.4) \times 10^{20}$ D/m^2, for 2h_sample, 8h_sample, 16h_sample, and 64h_sample, respectively. In general, the high concentration at depth of 1~7 μm is suggested to be attributed to blisters [6,39,41]. The rear of 64h_sample is measured by NRA but the signal is below the detection limit. Overall, D concentration in the shallow surface layer (0–7 μm) increases with exposure duration.

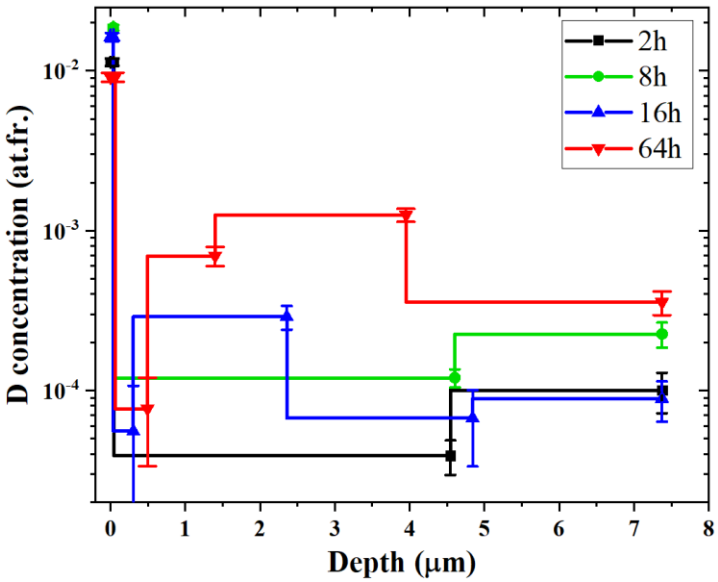

Figure 4. D depth profile of samples exposed to D plasmas at 500 K with a duration from 2 hours to 64 hours measured by ^{3}He NRA.

3.3. Thermal desorption spectra of deuterium

D desorption spectra are exhibited in figure 5. The desorption spectra show two distinct peaks in all cases. For both peaks, the peak intensity increases with fluence. With increasing exposure duration, the main peak position remains fixed at ~654 K, while the secondary peak gradually shifts from ~744 K to ~823 K, which is towards high temperatures. Sudden excursions of D signals in the low-temperature region of the spectra are visible and ascribed to the sudden blister ruptures during desorption [42]. Desorption at temperatures below the exposure temperature of 500 K is observed, which could be attributed to the fast cooling of exposed samples after the plasma is stopped.

The total D retention is calculated using desorption signal of D_2 and HD, which is 0.7, 1.4,

2.2, and 3.5×10^{21} m^{-2} for 2h_sample, 8h_sample, 16h_sample, and 64h_sample, respectively. As shown in figure 6, the dependence of D retention on the fluence Φ is close to $\Phi^{0.5}$, which meets the expectation based on the diffusion-limited trapping mechanism.

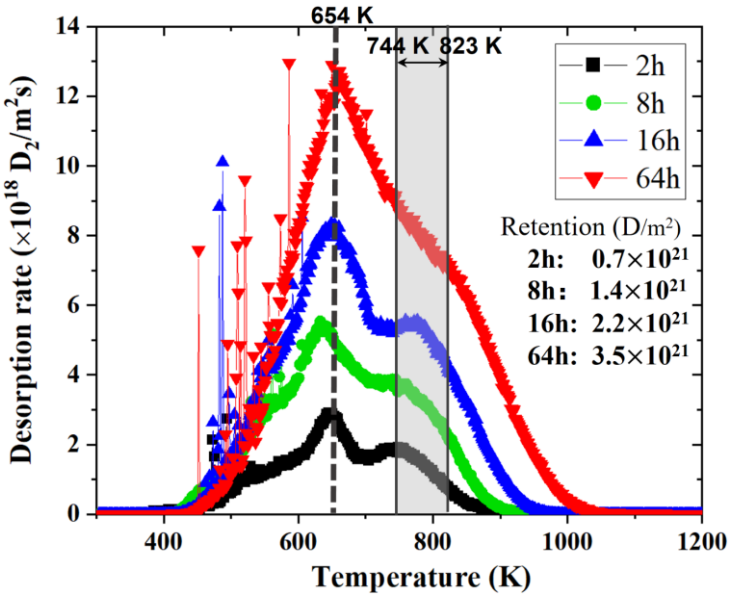

Figure 5. Thermal desorption spectra of the samples exposed to D plasma at 500 K for different durations in the range of 2 h to 64 h. All samples were heated with a linear heating ramp of 1 K/s from room temperature up to 1273 K. The main peaks are indicated by a black dotted line, and the secondary peak shifts from 744 K to 823 K and this range is indicated by a grey shaded area. The retention values are marked in the figure.

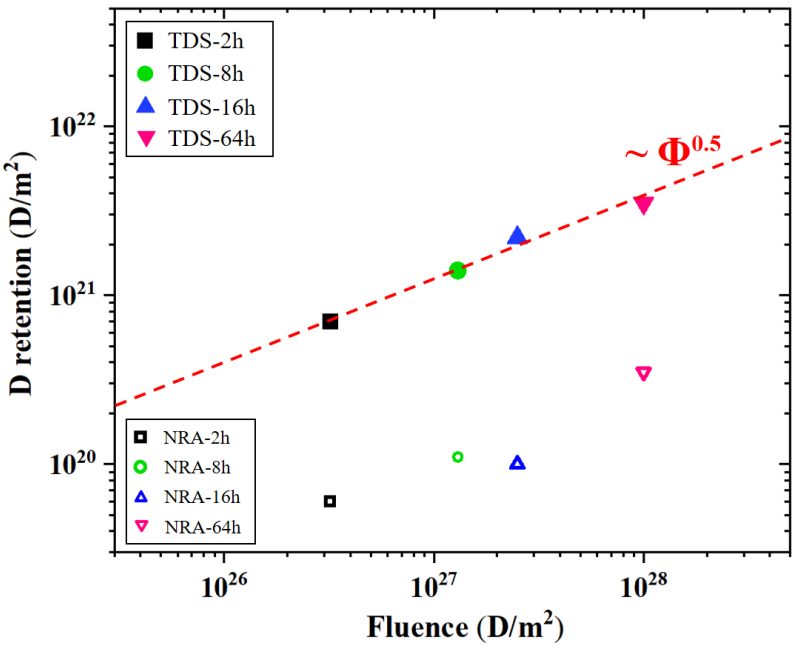

Figure 6. Retention measured by TDS and NRA as a function of the exposure fluence.

4. Discussion

4.1. Simulation of TDS using a uniform depth distribution of intrinsic defect

In the figure 6, the comparison between the total D retention derived from TDS and NRA measurement implies that a large part (>90%) of total retained D atoms are trapped in the bulk, that is at depth larger than 7 μm, which indicates a deep D trapping in the bulk. As defects induced by plasma ions are usually considered to be limited to a shallow sub-surface layer (~ a few μm) [3], the preliminary explanation to the large D retention in the bulk is trapping at intrinsic defects uniformly distributed in the bulk. As the base for analysis, the fluence dependence of TDS is simulated using TMAP based on this defect model.

We start with the model of a single intrinsic defect type. The typical concentration levels of intrinsic defects in W are of the order of 10^{-4} at.fr. [2,43]. Thus, the defect concentration is set to be 1×10^{-4} at.fr.. The maximum calculated diffusion depth of 2h_sample, 8h_sample, 16h_sample, and 64h_sample is then about 113 μm, 222 μm, 354 μm, and 561 μm, respectively. This is calculated by dividing the total retention by the trap concentration of 1×10^{-4} with the assumption of single atom occupancy of a trap. The detrapping energy of the defect is set to be 1.10 eV. The depth distribution of the defect and the simulated TDS are shown in figure 7. As the main feature, the desorption peak moves significantly towards high temperature (from 670 K to 830 K) with increasing fluence. Note that the maximum depth of the 64h_sample in this condition is 561 μm showing that permeation is not achieved, which agrees with the NRA measurement at the rear of the 64h_sample. In [44], ITER grade W samples were exposed to a series of high fluence plasma exposures at relatively high temperature to avoid blistering damage and the retention scales as the square root of time/fluence, which indicates a diffusion dominating retention uptake by filling intrinsic defects in W. Correspondingly, the TDS results show that a single desorption peak shifts obviously towards high temperature with fluence. This agrees with the simulated TDS in figure 7(b).

In a next step the model is modified to include two types of intrinsic defects based on the observation of two peaks in TDS measurement while keeping a uniform depth distribution at a

total concentration of 1×10^{-4} at.fr.. After fitting TDS profiles with two peaks using a Gaussian function, the area ratio of the main peak to the second peak is close to ~3.3 for four fluences. Then the concentration of defect 1 and defect 2 is set to be 7.7×10^{-5} at.fr. and 2.3×10^{-5} at.fr., respectively. The detrapping energy of defect 1 is again set to be 1.10 eV, the detrapping energy of defect 2 is set to be 1.35 eV. The simulated TDS result is shown in figure 8. Similar to the case of a single defect, in the dual defect model the main feature is the shift of the desorption peaks towards high temperatures with increasing fluence. Besides, the distinction between the two peaks becomes harder as the fluence increases.

It should be noted that the detrapping energies of 1.10 eV and 1.35 eV are values derived from the simulation in section 4.2. The difference between simulated spectrum with a same set of detrapping energies shows the impact of the defect depth distribution. Using a uniform depth distribution of defects, the main feature of desorption spectrum is the shift of the desorption peak towards high temperatures with increasing fluences, if the detrapping energy is kept constant. This peak shift can be understood by the delay of D arriving at the surface due to the longer migration path during desorption. As the desorption peak at ~650 K is almost immobile with changing fluences in the experimental TDS results, it indicates the failure of using the intrinsic defect model of a uniform depth distribution to explain the retention results.

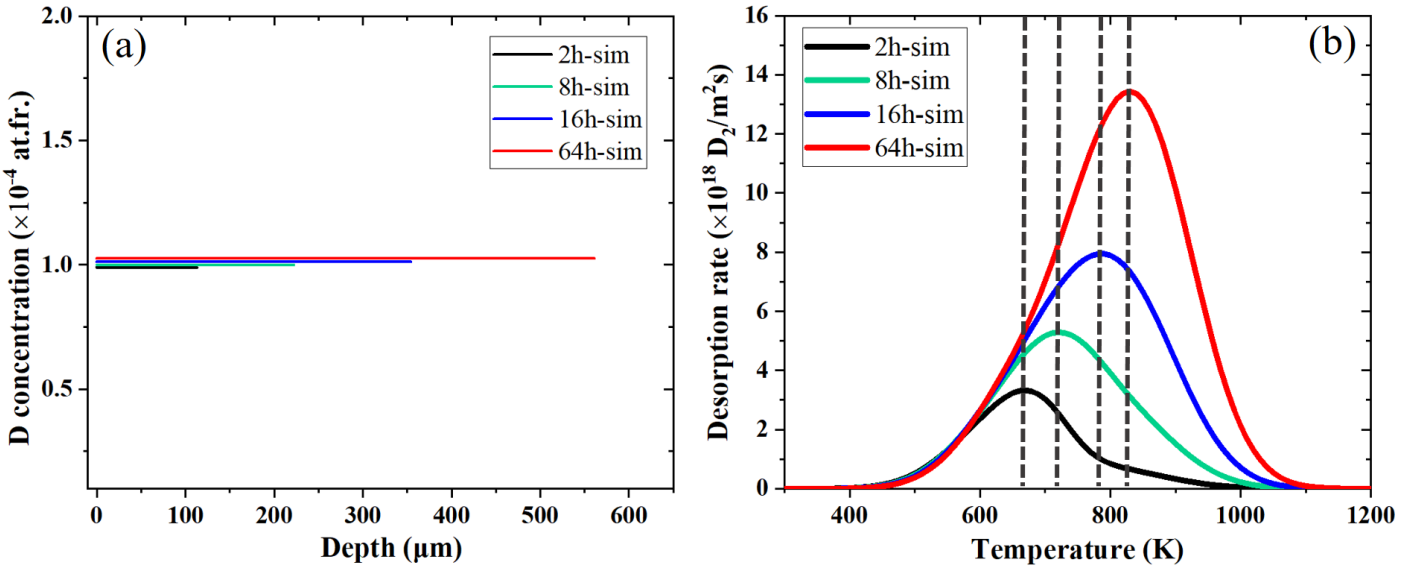

Figure 7. Simulation of thermal desorption spectra using the single intrinsic defect model of a uniform depth distribution for the defect. (a) The uniform depth distribution of D. (b) Simulated TDS by TMAP. The D

detrapping energy in the defect is 1.10 eV. Note that all D concentrations assumed in (a) are identical, but for view convenience, the tiny intervals among the lines are drawn to avoid overlapping.

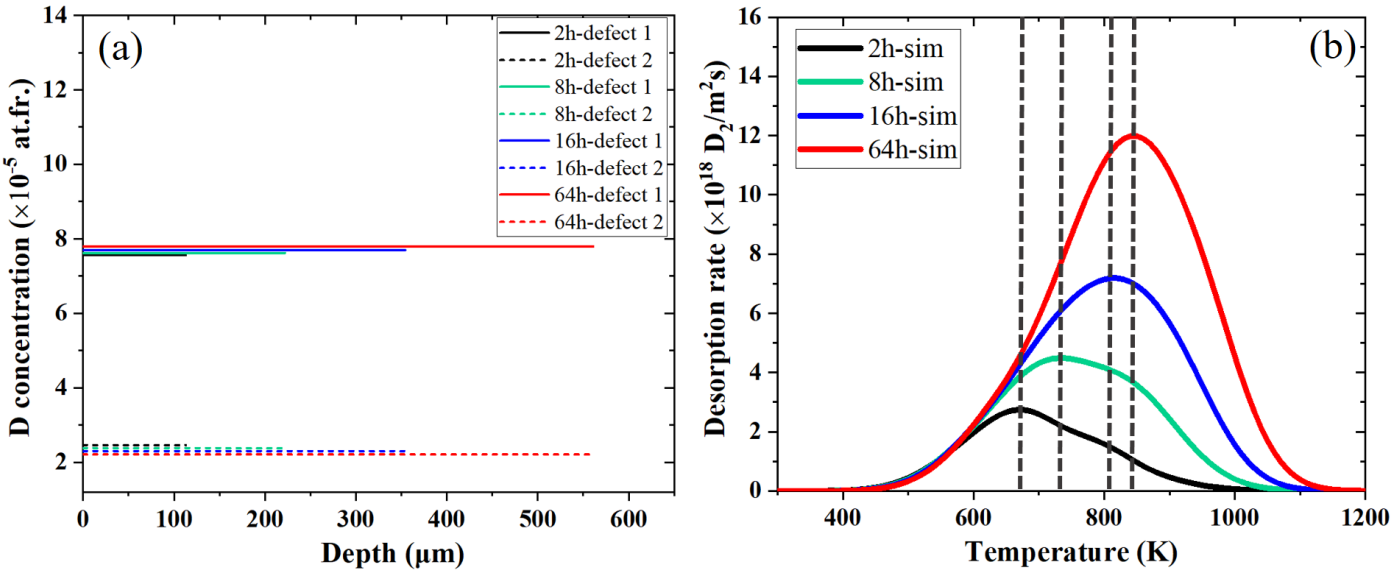

Figure 8. Simulation of thermal desorption spectra using two types of intrinsic defects with uniform depth distributions. (a) D concentration depth profile of two types of intrinsic defects with uniform depth distributions. (b) Simulated TDS by TMAP. The detrapping energies for defect 1 and defect 2 are 1.10 eV and 1.35 eV, respectively. D concentrations in (a) follows the same treatment as in the caption of figure 7.

4.2. Simulation of TDS using a depth distribution of defects

After the simulation solely based on the intrinsic defects with uniform depth distributions, the defect distribution is adjusted to account for the different distributions close to the surface and within the bulk.

After numerous attempts of adjusting detrapping energies and defect distribution, the simulation of experimental TDS is achieved as shown in figure 9, which uses two types of defects with detrapping energies of 1.10 eV and 1.35 eV and their depth distribution. In the depth distribution of the defects, two important features are observed. The first is that the defect concentration increases significantly with the fluence at depth less than ~40 μm, instead of staying constant. The other is that the defect profile has a sharp edge at ~40 μm, which separates the depth profile into two parts. For defect 1 with a detrapping energy of 1.10 eV, its concentration falls gradually from 1.4×10^{-3} to 2×10^{-4} at.fr. at depth less than 40 μm, but drops

to nearly 1×10^{-5} at.fr. at a depth larger than 40 μm. Because most of defect 1 is limited to a thickness of 40 μm, the position of the corresponding desorption peak stays relatively constant at ~650 K even if the fluence increases by a factor of 32. For defect 2, the concentration gradually falls at depth less than 40 μm. While at depth beyond 40 μm, the defect concentration reaches a saturation of $\sim9.0\times10^{-5}$ at.fr. but its maximum depth increases with the fluence, which accounts for the peak shift towards high temperature at ~800 K.

The solution to the simulation of an experimental TDS is in principle not unique, which is affected by detrapping energies and depth profiles of defects. While judging from the evolution of desorption peaks with fluences and the values of detrapping energies (as shown in section 4.3), the depth profiles proposed in figure 9 is considered as the most probable solution. Besides, the simulated depth profile matches the retentions measured by NRA and TDS. Firstly, the average concentration at a depth of 10 μm in the simulated profile is in line with the average value in the NRA measurement. And defect concentrations at depth beyond 10 μm agree with the fact that the majority of D atoms are trapped at depth beyond 7 μm as shown in figure 6.

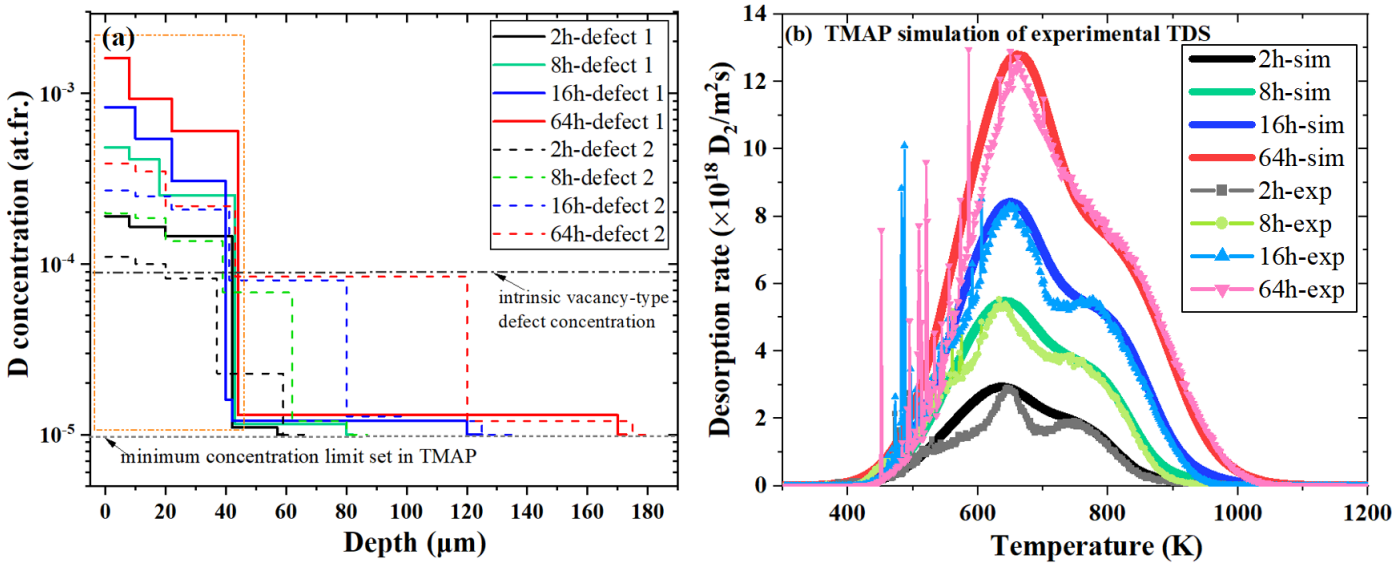

Figure 9. Simulated D concentration depth profile (a) and the simulated TDS (b). Note that the Y-axis is plotted in logarithmic scale in (a). The comparison between the simulated TDS and the experimental TDS is included in (b). The detrapping energies for defect 1 and defect 2 are 1.10 eV and 1.35 eV, respectively.

4.3. Defect characterization

Although the simulated defect distributions in section 4.2 are in line with TDS measurement, the nature of the defects needs to be clarified. The TMAP simulations indicate that most defects are not intrinsic defects and caused by plasma irradiation. However, the simulated irradiation-induced defects with a depth distribution over ~40 μm require further investigation, because irradiation-induced defects such as superabundant vacancies [45] are generally considered to be limited to shallow depth at a few microns.

The development of blistering shown in figure 2 is considered as a major source of irradiation-induced defects. D_2 molecules trapped by blisters are generally considered to contribute to D retention [7,39]. Recent TEM investigations of irradiation-induced defects near blistering [8,46,47] show the production of dislocation-type defects, indicating a potential contribution to D trapping. The idea of blister-relevant trapping is examined in this section.

4.3.1. Major retention not from D_2 molecules in the blister cavities

D atoms or D_2 molecules in the cavity associated with a blister are generally regarded as the effect of blister on D retention [7,39]. However, this is not likely the main source of D retention in this study. As measured in the cross-section of blisters, cavities are usually located at a depth of ~5 μm (figure 3) which is covered by the probing depth of NRA. This means that the number of D atoms or D_2 molecules in blister-relevant cavities is not more than that detected by NRA. Besides, the observed blister bursting is a general observation in high fluence case in figure 2, and indicates a possible loss channel for D_2 molecules rather than an incremental contribution to retention. In fact, the highest retention is observed in the 64h_sample in which most blisters on the surface burst, indicating a limited contribution of D_2 molecules retained in cavities to the total retention. Manhard *et al* suggested that the D release from blister bursting of low flux D exposures of polycrystalline tungsten at 370 K only accounted for 3–5% of the total D retention [42]. Therefore, the major contribution trapped by defects is unlikely D_2 molecules retained in cavities.

4.3.2. Blister-induced dislocation-type defects

In recent studies of blister-induced damage in the W matrix, dislocation-type defects are widely investigated and discussed [8,9,48]. These defects are the product of the matrix deformation during blistering. Considering the D detrapping energy at dislocations is in the range of 0.85–1.25 eV [25,49,50], defect 1 with detrapping energy 1.10 eV in section 4.2 is

speculated to be of dislocation-type defect.

In order to further verify the speculation, a dedicated TEM sample was exposed to D plasma at STEP to create blisters. Before exposure, no clear defect is observed as shown in figure 10(a). Because dense dislocations are expected in the blister cap due to plastic deformation, the blister cap is removed via electrochemical polishing after exposure. A very dense network of dislocations or dislocation tangles is observed near a blister cap in figure 10(b) and 10(c). The highest density of dislocations is located at the blister edge which has suffered from the most severe deformation.

In figure 10(b), it is observed that the dislocations are distributed throughout the surface and a few dislocations are ~ 3 μm away from the blister edge. This indicates that the blister-induced dislocations would not stay in the confined area of the bottom of blister cap but could move away from blister. This is the result of the dislocation slide under stress, which could be facilitated by the presence of HI [51–53]. That is to say, blister-induced dislocations could possibly slip towards the bulk. In fact, depth distribution of dislocations extending deep into the material originating from blisters has been observed in a large cross-section by TEM in recent experiments [46,48]. Generally, blister-induced defects are considered to be close to the cavity, i.e., the cavity depth is regarded as the defect depth. However, Chen *et al* [46] recently demonstrated that cavity/blister formations in recrystallized W could emit substantial dislocation loops into the bulk, resulting in the diffusion depth of blister-induced dislocations much larger than the cavity depth. Thus these dislocations turn out to be diffusive defects which provides an important support for the simulated large depth distribution of defect 1 in figure 9(a). The depth distribution of dislocations in [46] shows a decrease of concentration with depth, which supports our simulated depth distribution. Besides, considering the large exposure duration and fluence compared with that in [46], dislocations in this study are expected to reach even a larger depth.

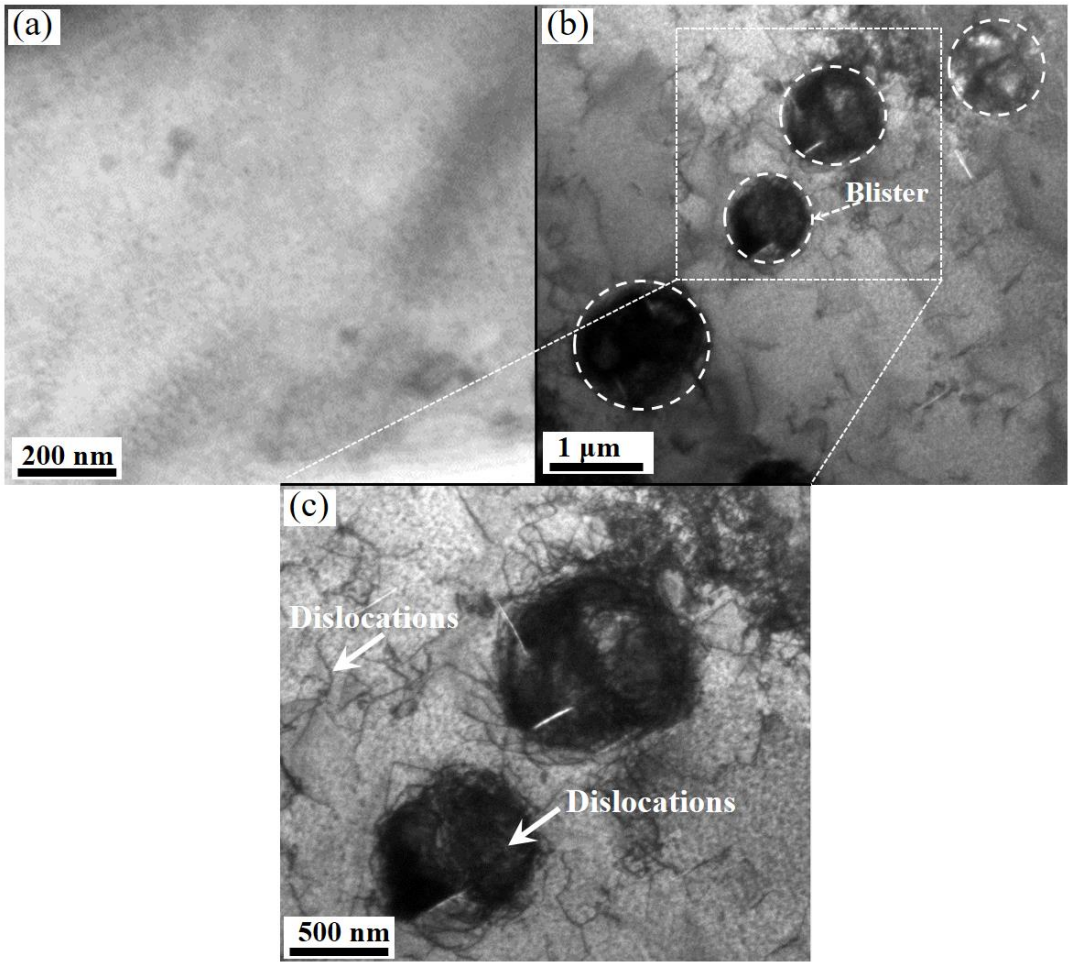

Figure 10. TEM images of the pristine microstructure in the unexposed TEM specimen (a), microstructures of blisters in the specimen exposed to plasma with a fluence of 1.0×10^{26} m^{-2} (b), and an enlarged view of microstructures (c). Blister microstructures are indicated by white dashed circles in (b). The dislocations are distributed throughout the specimen and a few dislocations are about 3 μm away from the blister edge in (b). The microstructure of a blister consists of dense dislocation tangles similar to a ball of black wool. The dislocations are pointed by white solid arrows in (c).

A dislocation is usually terminated at or absorbed by sinks such as surfaces or interfaces [54,55]. Because pure W samples are used, the sharp edge at ~40 μm is considered as the first interface that dislocations could encounter, which should be the first layer of grain boundaries (GBs) parallel to the surface. The effect of GB on the dislocation sliding is unfolded by TEM observation as shown in figure 11. The GB is a clear boundary of the matrix with and without dislocations, thus blister-induced dislocations are all limited on one side of GB and can not cross over to the other side. Furthermore, 40 μm is very close to the average grain size measured

on the surface in figure 1. In fact, if we check the lateral fracture surface as shown in figure 12, the average depth of the first layer of GBs is ~33 μm away from the exposed surface, which is close to 40 μm. This serves as another support for the identification of defect 1 as the dislocation-type defect.

The defect 1 at a depth beyond 40 μm in figure 9(a) is considered to be intrinsic dislocation-type defect in W, but its concentration is very low close to the minimum value set in TMAP simulation of this study. This agrees well with the TEM observation of no clear dislocation defects in the unexposed specimen (figure 10(a)) due to high temperature annealing. Thus, the contribution of intrinsic dislocation-type defects to retention is negligible.

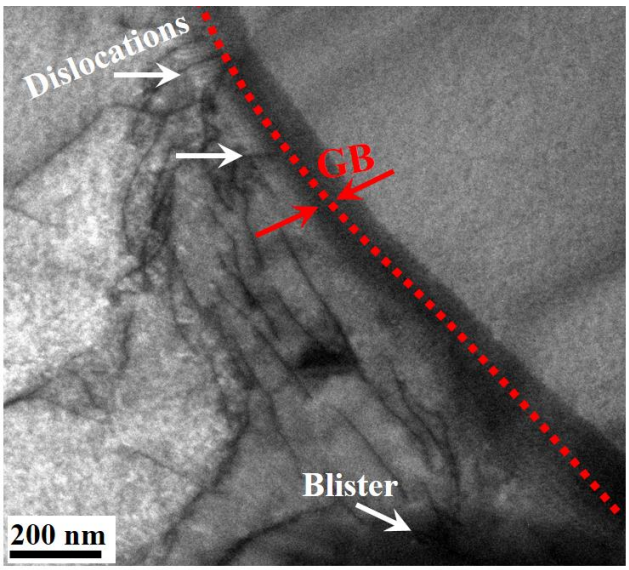

Figure 11. TEM image of blister-induced dislocations near a GB. As dislocations are not visible on the other side of the GB, it indicates that the movement of dislocations is hindered by the GB.

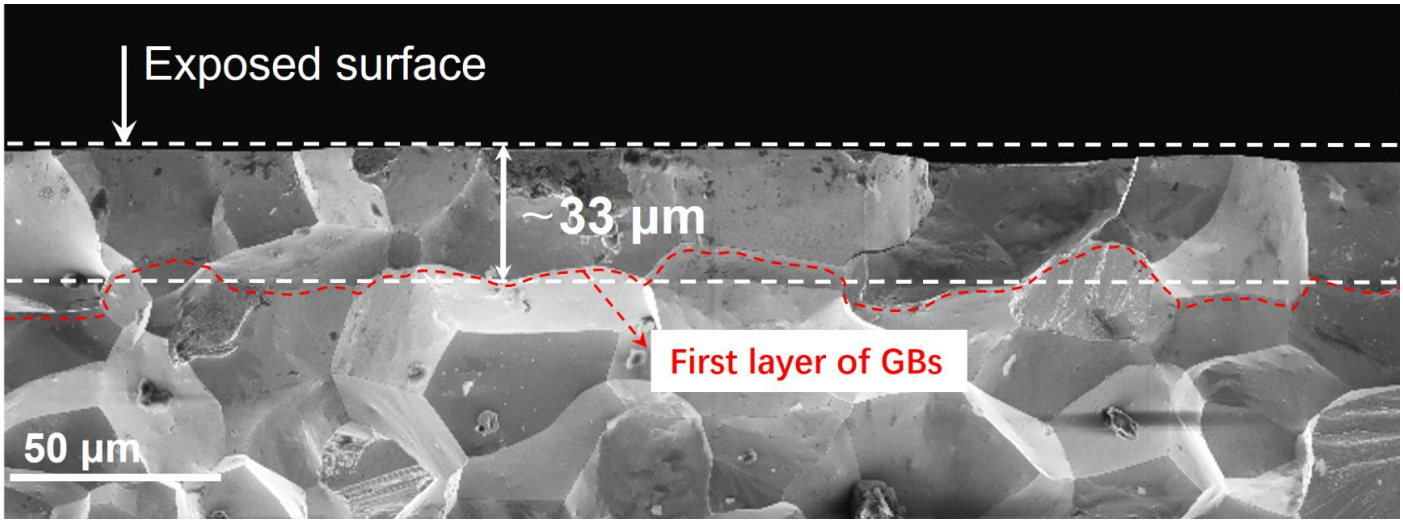

Figure 12. SEM image of the lateral fracture surface of W bulk, which is vertical to the exposed surface. The first layer of GBs is marked by a red dashed line. The average distance between the first layer of GBs and the exposed surface is ~33 μm.

4.3.3. Blister-induced vacancy-type defects

The detrapping energy of defect 2 falls in the range of that of a vacancy-type defect [56]. The simulated concentration of defect 2 close to the surface increases with exposure duration as shown in figure 9(a). To verify this simulation result, PADB was used to detect the vacancy-type defect in the exposed samples. As shown in figure 13, the PADB result exhibits an increase of S parameter with exposure duration, which indicates the growth of the vacancy population with exposure duration. Although the D incident energy is much less than the damage threshold (~900 eV) to displace W atom [57], the generation of the vacancy-type defect by low energy and high flux D plasma was found by PADB in many experiments [36,37,58,59]. The reason for vacancy formation is often suggested to be D supersaturation in W [36,60,61]. As H in W could reduce the vacancy formation energy [62,63], a spontaneous formation of mono-vacancy will occur when the ratio of H atoms over W atoms exceeds 0.5 [64].

Here, we suggest that the vacancy-type defects should be created by blistering. In the literatures [36,37,58,59], the vacancy-type defect formation is correlated with blistering. This is because vacancy-type defects can be produced via blister-induced dislocations with the help of two formation mechanisms [65,66]. The first is that when two dislocations with opposite Burgers vectors intersect with each other which would separate their glide planes by one or more interatomic distances, a row of vacancy-type defects will be produced. The second is that the motion of a screw dislocation along with a jog could lead to the generation of a row of vacancy-type defects, and this generation process is favoured because the presence of HI can reduce the vacancy formation energy. This explanation of vacancy defect generation via dislocation intersection and motion can agree well with the observation that both of defect 1 and defect 2 have a similar depth distribution at depth less 40 μm in figure 9(a). It should be noted that the S parameter of 2h_sample remains relatively unchanged compared to that of the non-exposed sample. This is in line with the observation of a small amount of blister on the surface, thus supports the proposed relationship between blisters and vacancies.

As for the sharp edge at ~40 μm in the depth profile of defect 2, the first layer of GBs could also obstruct the transportation of vacancy defects. Thus, the defect 2 at depth beyond 40 μm should be attributed to intrinsic vacancy-type defect in the bulk. This explains why the defect 2 concentration reaches a saturation value of ~9.0×10^{-5} at.fr., but the diffusion front is extended over the exposure duration.

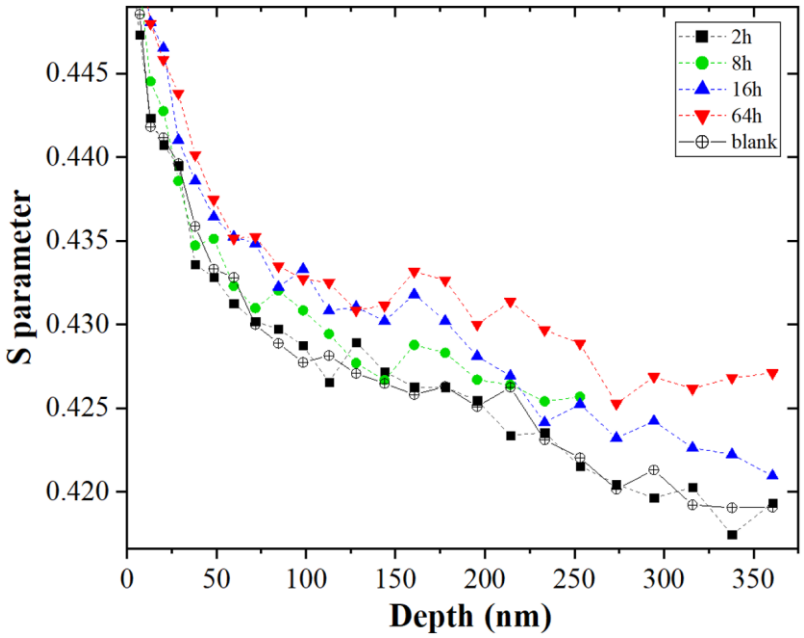

Figure 13. PADB of samples after plasma exposure with a duration from 2 h to 64 h at 500 K. The result from a non-exposed sample is also included.

4.4. Blister-dominated retention mechanism

Based on the discussion in section 4.3, defects 1 and 2 in the TDS simulation are suggested to be the dislocation-type defect and the vacancy-type defect, respectively. The defects induced by plasma exposure are suggested to be associated with the formation of blisters, and consist of dislocation-type defects and part of vacancy-type defects that are related to blistering. Following the simulated depth profile in figure 9(a), the contribution of blister-induced defects and intrinsic defects to D retention is calculated and plotted in figure 14. The D retained in blister-induced dislocation-type defects and the blister-induced vacancy-type defects accounts for at least ~63% and ~14% of the total retention, respectively, for all exposure durations. Thus, the percentage of retention trapped at blister-induced defects accounts for more than 77% of the

total retention and the rest accounts for less than 23%. In addition, as shown in figure 14 the blister density (number/m^2) is counted and compared with the amount of D trapped by blister-induced defects in the simulated profile. This comparison shows a positive correlation between each, which implies blister-related trapping processes. To account for the contribution of blistering to D retention, we propose a blister-dominated retention mechanism if the plasma exposure condition permits severe blistering. The schematic diagram of this mechanism including defect growth, defect distribution and D trapping is shown in figure 15.

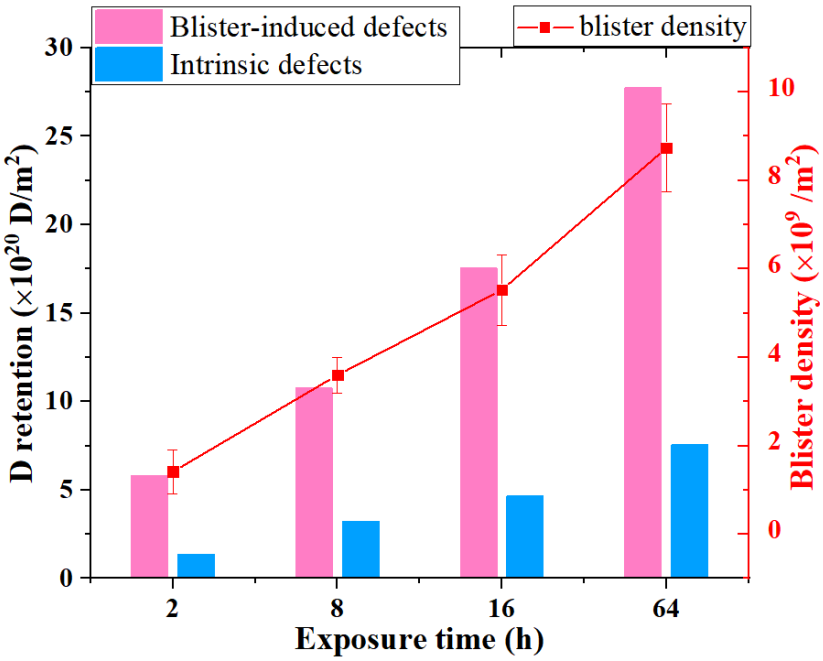

Figure 14. D retention in blister-induced defects and intrinsic defects as identified in the simulated depth profile in figure 9(a). The blister density on the surface is counted and plotted as well for the comparison with D trapping by the simulated blister-induced defects.

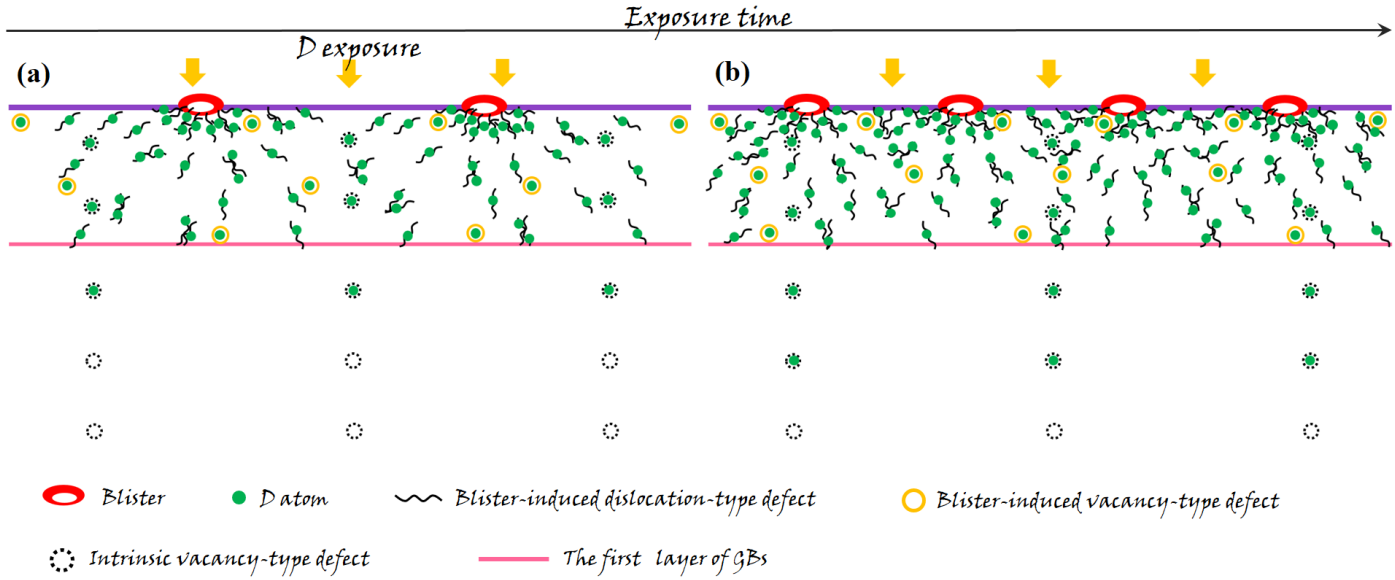

Figure 15. Schematic diagram of the proposed blister-dominated retention mechanism. (a) When blistering happens, many dislocation-type defects and vacancy-type defects are generated to attract a large part of incoming D atoms and the intrinsic defects absorb a small part of incoming D atoms. (b) As exposure time/fluence increases, the more blisters create more dislocation-type defects and vacancy-type defects to enhance absorption of incoming D atoms and the more deep intrinsic defects are also filled by D atoms due to increasing diffusion depth. In (a) and (b), the density of blister-induced defects is much higher than that of intrinsic defects, resulting in a blister-dominated retention. Besides, the blister-induced defects would diffuse into bulk, but would be limited in the first layer of grains due to that their movement is hindered by the first layer of GBs, which results in that majority of retention is located in the surface layer of a certain thickness.

5. Conclusion

In this work, a series of D plasma exposures with fluences from 3.2×10^{26} to 1.0×10^{28} ions/m^2 were performed at 500 K using recrystallized W samples. It is found that surface blistering, D concentration measured by NRA and total D retention measured by TDS increase with the fluence.

D desorption spectra were simulated using TMAP to investigate the binding energy and depth profile of defects. The TDS simulation suggested that the irradiation-induced defects are related to blistering and consist of the dislocation-type defects and the vacancy-type defects, which are the major contribution to total D retention. The simulated depth profile of the irradiation-induced defects features a large depth distribution of ~40 μm, indicating the

irradiation-induced defects, especially the dislocation-type defects could be diffusive and result in a deep distribution of the defects. To account for the potential contribution of blistering to D retention, a blister-dominated retention mechanism is proposed to model D retention.

Acknowledgments

This work is supported by the National Nature Science Foundation of China under Grant 51720105006, 11805007, and 11675009, and the Users with Excellence Project of Hefei Science Center of CAS under Grant 2018HSC-UE006. The author would like to thank Pengfei Hou and Yida Zhu for their technical support in the STEP experiment. The views and opinions expressed herein do not necessarily reflect those of the ITER Organization.

References

[1] Lu G-H, Zhou H-B and Becquart C S 2014 A review of modelling and simulation of hydrogen behaviour in tungsten at different scales *Nucl. Fusion* **54** 086001

[2] De Temmerman G, Hirai T and Pitts R A 2018 The influence of plasma-surface interaction on the performance of tungsten at the ITER divertor vertical targets *Plasma Phys. Control. Fusion* **60** 044018

[3] Ueda Y, Schmid K, Balden M, Coenen J W, Loewenhoff T, Ito A, Hasegawa A, Hardie C, Porton M and Gilbert M 2017 Baseline high heat flux and plasma facing materials for fusion *Nucl. Fusion* **57** 092006

[4] Morgan T W, Balden M, Schwarz-Selinger T, Li Y, Loewenhoff T H, Wirtz M, Brezinsek S and De Temmerman G 2020 ITER monoblock performance under lifetime loading conditions in Magnum-PSI *Phys. Scr.* **T171** 014065

[5] Jia Y Z, De Temmerman G, Luo G N, Xu H Y, Li C, Fu B Q and Liu W 2015 Surface morphology and deuterium retention in tungsten exposed to high flux D plasma at high temperatures *J. Nucl. Mater.* **457** 213–9

[6] Zibrov M, Balden M, Morgan T W and Mayer M 2017 Deuterium trapping and surface modification of polycrystalline tungsten exposed to a high-flux plasma at high fluences *Nucl. Fusion* **57** 046004

[7] Balden M, Manhard A and Elgeti S 2014 Deuterium retention and morphological modifications of the surface in five grades of tungsten after deuterium plasma exposure *J. Nucl. Mater.* **452** 248–56

[8] Guo W, Ge L, Yuan Y, Cheng L, Wang S, Zhang X and Lu G-H 2019 <001> edge dislocation nucleation mechanism of surface blistering in tungsten exposed to deuterium plasma *Nucl. Fusion* **59** 026005

[9] Manhard A, von Toussaint U, Balden M, Elgeti S, Schwarz-Selinger T, Gao L, Kapser S, Płociński T, Grzonka J, Gloc M and Ciupiński 2017 Microstructure and defect analysis in the vicinity of blisters in polycrystalline tungsten *Nucl. Mater. Energy* **12** 714–9

[10] Bakaev A, Grigorev P, Terentyev D, Bakaeva A, Zhurkin E E and Mastrikov Y A 2017 Trapping of hydrogen and helium at dislocations in tungsten: an ab initio study *Nucl. Fusion* **57** 126040

[11] Terentyev D, Dubinko V, Bakaev A, Zayachuk Y, Van Renterghem W and Grigorev P 2014 Dislocations mediate hydrogen retention in tungsten *Nucl. Fusion* **54** 042004

[12] De Backer A, Mason D R, Domain C, Nguyen-Manh D, Marinica M C, Ventelon L, Becquart C S and Dudarev S L 2018 Multiscale modelling of the interaction of hydrogen with interstitial defects and dislocations in BCC tungsten *Nucl. Fusion* **58** aa8e0c

[13] Zhu X L, Cheng L, De Temmerman G, Shi L Q, Yuan Y, Wang B Y, Cao X Z, Lu E Y, Zhang Y and Lu G H 2017 Effects of stress-relief pre-annealing on deuterium trapping and diffusion in tungsten *Fusion Eng. Des.* **125** 526–30

[14] Lu G-H, Cheng L, Arshad K, Yuan Y, Wang J, Qin S, Zhang Y, Zhu K, Luo G-N, Zhou H, Li B, Wu J and Wang B 2017 Development and Optimization of STEP—A Linear Plasma Device for Plasma-Material Interaction Studies *Fusion Sci. Technol.* **71** 177–86

[15] Yin H, Wang J, Guo W, Cheng L, Yuan Y and Lu G 2019 Recent studies of tungsten-based plasma-facing materials in the linear plasma device STEP *Tungsten* **1** 132–40

[16] Mayer M, Gauthier E, Sugiyama K and von Toussaint U 2009 Quantitative depth profiling of deuterium up to very large depths *Nucl. Instruments Methods Phys. Res. Sect. B Beam Interact. with Mater. Atoms* **267** 506–12

[17] Schmid K and Von Toussaint U 2012 Statistically sound evaluation of trace element depth profiles by ion beam analysis *Nucl. Instruments Methods Phys. Res. Sect. B Beam*

Interact. with Mater. Atoms **281** 64–71

[18] Zhu X-L, Zhang Y, Kreter A, Shi L-Q, Yuan Y, Cheng L, Linsmeier C and Lu G-H 2018 Aggravated blistering and increased deuterium retention in iron-damaged tungsten after exposure to deuterium plasma with various surface temperatures *Nucl. Fusion* **58** 106005

[19] Longhurst G.R. 2008 TMAP7 user manual Idaho National Engineering and Environment Laboratory (Idaho Falls,Idaho) INEEL/EXT-04-02352(Rev. 2)

[20] Shimada M and Taylor C N 2019 Improved tritium retention modeling with reaction-diffusion code TMAP and bulk depth profiling capability *Nucl. Mater. Energy* **19** 273–8

[21] Shimada M, Oya Y, Wampler W R, Yamauchi Y, Taylor C N, Garrison L M, Buchenauer D A and Hatano Y 2018 Deuterium retention in neutron-irradiated single-crystal tungsten *Fusion Eng. Des.* **136** 1161–7

[22] Baldwin M J, Doerner R P, Nishijima D, Patino M, Simmonds M J, Tynan G, Yu J H and Založnik A 2019 Plasma-Material-Interaction Research Using PISCES Linear Plasma Devices *Fusion Sci. Technol.* **75** 664–73

[23] Baldwin M J and Doerner R P 2017 Hydrogen isotope transport across tungsten surfaces exposed to a fusion relevant He ion fluence *Nucl. Fusion* **57** 076031

[24] Merrill B J, Shimada M and Humrickhouse P W 2013 Simulating Tritium Retention in Tungsten with a Multiple Trap Model in the TMAP Code *Plasma Fusion Res.* **10** 71–5

[25] Wright G M, Mayer M, Ertl K, de Saint-Aubin G and Rapp J 2011 TMAP7 simulations of deuterium trapping in pre-irradiated tungsten exposed to high-flux plasma *J. Nucl. Mater.* **415** S636–40

[26] Poon M, Haasz A A and Davis J W 2008 Modelling deuterium release during thermal desorption of D+-irradiated tungsten *J. Nucl. Mater.* **374** 390–402

[27] Frauenfelder R 1969 Solution and Diffusion of Hydrogen in Tungsten *J. Vac. Sci. Technol.* **6** 388–97

[28] Ogorodnikova O V 2019 Recombination coefficient of hydrogen on tungsten surface *J. Nucl. Mater.* **522** 74–9

[29] Schmid K 2016 Diffusion-trapping modelling of hydrogen recycling in tungsten under ELM-like heat loads *Phys. Scr.* **T167** 014025

[30] Causey R A 2002 Hydrogen isotope retention and recycling in fusion reactor plasma-

facing components *J. Nucl. Mater.* **300** 91–117

[31] Fernandez N, Ferro Y and Kato D 2015 Hydrogen diffusion and vacancies formation in tungsten: Density Functional Theory calculations and statistical models *Acta Mater.* **94** 307–18

[32] Johnson D F and Carter E A 2010 Hydrogen in tungsten: Absorption, diffusion, vacancy trapping, and decohesion *J. Mater. Res.* **25** 315–27

[33] Schmid K, Von Toussaint U and Schwarz-Selinger T 2014 Transport of hydrogen in metals with occupancy dependent trap energies *J. Appl. Phys.* **116**

[34] Zhu X-L, Zhang Y, Cheng L, Yuan Y, De Temmerman G, Wang B-Y, Cao X-Z and Lu G-H 2016 Deuterium occupation of vacancy-type defects in argon-damaged tungsten exposed to high flux and low energy deuterium plasma *Nucl. Fusion* **56** 036010

[35] Wang S, Guo W, Yuan Y, Gao N, Zhu X, Cheng L, Cao X, Fu E, Shi L, Gao F and Lu G-H 2020 Evolution of vacancy defects in heavy ion irradiated tungsten exposed to helium plasma *J. Nucl. Mater.* **532** 152051

[36] Xu H Y, Luo G N, Schut H, Yuan Y, Fu B Q, Godfrey A, Liu W and Temmerman G De 2014 Enhanced modification of tungsten surface by nanostructure formation during high flux deuterium plasma exposure *J. Nucl. Mater.* **447** 22–7

[37] Shu W M, Kawasuso A and Yamanishi T 2009 Recent findings on blistering and deuterium retention in tungsten exposed to high-fluence deuterium plasma *J. Nucl. Mater.* **386–388** 356–9

[38] Bao-Yi W, Yan-Yun M, Ping W, Xing-Zhong C, Xiu-Bo Q, Zhe Z, Run-Sheng Y and Long W 2008 Development and application of the intense slow positron beam at IHEP *Chinese Phys. C* **32** 156–9

[39] Alimov V K, Shu W M, Roth J, Lindig S, Balden M, Isobe K and Yamanishi T 2011 Temperature dependence of surface topography and deuterium retention in tungsten exposed to low-energy, high-flux D plasma *J. Nucl. Mater.* **417** 572–5

[40] Cheng L, De Temmerman G, Morgan T W, Schwarz-Selinger T, Yuan Y, Zhou H B, Wang B, Zhang Y and Lu G H 2017 Mitigated blistering and deuterium retention in tungsten exposed to high-flux deuterium–neon mixed plasmas *Nucl. Fusion* **57** 046028

[41] ’t Hoen M H J, Balden M, Manhard A, Mayer M, Elgeti S, Kleyn A W and Zeijlmans

van Emmichoven P A 2014 Surface morphology and deuterium retention of tungsten after low- and high-flux deuterium plasma exposure *Nucl. Fusion* **54** 083014

[42] Manhard A, Toussaint U v, Dürbeck T, Schmid K and Jacob W 2011 Statistical analysis of blister bursts during temperature-programmed desorption of deuterium-implanted polycrystalline tungsten *Phys. Scr.* **T145** 014038

[43] Schmid K, Bauer J, Schwarz-Selinger T, Markelj S, Toussaint U V., Manhard A and Jacob W 2017 Recent progress in the understanding of H transport and trapping in W *Phys. Scr.* **T170** 014037

[44] Doerner R P, Baldwin M J, Lynch T C and Yu J H 2016 Retention in tungsten resulting from extremely high fluence plasma exposure *Nucl. Mater. Energy* **9** 89–92

[45] Fukai Y 2003 Formation of superabundant vacancies in M–H alloys and some of its consequences: a review *J. Alloys Compd.* **356–357** 263–9

[46] Chen W Q, Wang X Y, Chiu Y L, Morgan T W, Guo W G, Li K L, Yuan Y, Xu B and Liu W 2020 Growth mechanism of subsurface hydrogen cavities in tungsten exposed to low-energy high-flux hydrogen plasma *Acta Mater.* **193** 19–27

[47] Manhard A and Gao L 2018 Blisters formed by D plasma exposure in an electron-transparent tungsten sample *Nucl. Mater. Energy* **17** 248–52

[48] Chen W Q, Xiao X Z, Pang B, Si S S, Jia Y Z, Xu B, Morgan T W, Liu W and Chiu Y L 2019 Irradiation hardening induced by blistering in tungsten due to low-energy high flux hydrogen plasma exposure *J. Nucl. Mater.* **522** 11–8

[49] Ogorodnikova O V., Roth J and Mayer M 2008 Ion-driven deuterium retention in tungsten *J. Appl. Phys.* **103** 034902

[50] Manhard A 2012 Deuterium inventory in tungsten after plasma exposure: a microstructural survey PhD Thesis Universität Augsburg (Report IPP 17/34, Max-PlanckInstitut für Plasmaphysik, Garching) (http://pubman.mpdl.mpg.de/pubman/item/escidoc:2146108/component/escidoc:214607/IPP_17_34.2.pdf)

[51] Itakura M, Kaburaki H, Yamaguchi M and Okita T 2013 The effect of Hydrogen atom on the Screw Dislocation Mobility in BCC Iron: A First-Principles Study *Acta Mater.* **61** 6857–67

[52] I.M R 2001 The effect of hydrogen on dislocation dynamics *Eng. Fract. Mech.* **68** 671–92

[53] Birnbaum H K and Sofronis P 1994 Hydrogen-enhanced localized plasticity-a mechanism for hydrogen-related fracture *Mater. Sci. Eng. A* **176** 191–202

[54] Dewald M P and Curtin W A 2007 Multiscale modelling of dislocation/grain boundary interactions. II. Screw dislocations impinging on tilt boundaries in Al *Philos. Mag.* **87** 4615–41

[55] Peng X-L and Huang G-Y 2015 Modeling dislocation absorption by surfaces within the framework of strain gradient crystal plasticity *Int. J. Solids Struct.* **72** 98–107

[56] Zibrov M, Ryabtsev S, Gasparyan Y and Pisarev A 2016 Experimental determination of the deuterium binding energy with vacancies in tungsten *J. Nucl. Mater.* **477** 292–7

[57] Jia Y Z, Liu W, Xu B, Qu S L, Shi L Q and Morgan T W 2017 Subsurface deuterium bubble formation in W due to low-energy high flux deuterium plasma exposure *Nucl. Fusion* **57** 034003

[58] Shu W M, Kawasuso A, Miwa Y, Wakai E, Luo G-N and Yamanishi T 2007 Microstructure dependence of deuterium retention and blistering in the near-surface region of tungsten exposed to high flux deuterium plasmas of 38 eV at 315 K *Phys. Scr.* **T128** 96–9

[59] Xu H Y, De Temmerman G, Luo G-N, Jia Y Z, Yuan Y, Fu B Q, Godfrey A and Liu W 2015 Deuterium-induced nanostructure formation on tungsten exposed to high-flux plasma *J. Nucl. Mater.* **463** 308–11

[60] Gao L, Jacob W, von Toussaint U, Manhard A, Balden M, Schmid K and Schwarz-Selinger T 2017 Deuterium supersaturation in low-energy plasma-loaded tungsten surfaces *Nucl. Fusion* **57** 016026

[61] Zayachuk Y, 't Hoen M H J, Zeijlmans van Emmichoven P A, Terentyev D, Uytdenhouwen I and van Oost G 2013 Surface modification of tungsten and tungsten–tantalum alloys exposed to high-flux deuterium plasma and its impact on deuterium retention *Nucl. Fusion* **53** 013013

[62] Liu Y-N, Ahlgren T, Bukonte L, Nordlund K, Shu X, Yu Y, Li X-C and Lu G-H 2013 Mechanism of vacancy formation induced by hydrogen in tungsten *AIP Adv.* **3** 122111

[63] Middleburgh S C, Voskoboinikov R E, Guenette M C and Riley D P 2014 Hydrogen induced vacancy formation in tungsten *J. Nucl. Mater.* **448** 270–5

[64] Xiao W, Luo G-N and Geng W T 2012 Threshold concentration for H blistering in defect free W *J. Nucl. Mater.* **421** 176–80

[65] Zhou S J, Preston D L and Louchet F 1999 Investigation of vacancy formation by a jogged dissociated dislocation with large-scale molecular dynamics and dislocation energetics *Acta Mater.* **47** 2695–703

[66] Zibrov M, Balden M, Dickmann M, Dubinko A, Egger W, Mayer M, Terentyev D and Wirtz M 2019 Deuterium trapping by deformation-induced defects in tungsten *Nucl. Fusion* **59** 106056